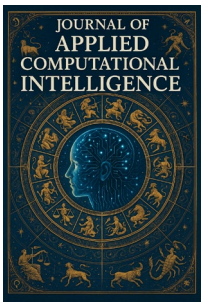
UNIVERSITY OF WEST ATTICA

eISSN: 3136-6937

Journal of Applied Computational Intelligence

Vol. 4, No. 1, January, 2026



Complex Valued U Net with Pupil Self Calibration for Fourier Ptychographic Reconstruction

Szűcs Csanád[1,*], Horváth Zsuzsanna[1]

[1] *Faculty of Electrical Engineering and Informatics, Budapest University of Technology and Economics, Budapest, 1117, Hungary*

Received 11 November 2025; Revised 10 March 2026; Accepted 12 March 2026; Published 15 March 2026

Abstract

Pupil aberrations introduce coupled amplitude and phase errors into Fourier ptychographic reconstruction, limiting the reliability of learned estimators when acquisition conditions depart from their training distribution. This study proposes a complex-valued U-Net that integrates pupil self-calibration with a differentiable coherent imaging operator. The object branch processes real and imaginary features through coupled convolutions, while a constrained pupil branch estimates low order aberration coefficients from measurement residuals. Alternating updates, pupil support constraints, and explicit phase gauge fixing separate optical correction from object refinement. The evaluation addresses reconstruction accuracy, aberration tolerance, measurement efficiency, and computational cost within a unified comparison protocol. The proposed configuration reaches an amplitude peak signal to noise ratio of 34.8 dB, a structural similarity index of 0.961, and an aligned phase root mean square error of 0.118 rad. The fixed pupil complex network reaches 31.2 dB and 0.187 rad under the same comparison settings. Removing pupil calibration increases pupil phase error from 0.072 to 0.241 rad. Joint analysis of object error, coefficient trajectories, and held out illumination residuals characterizes the interaction between the learned specimen representation and acquisition specific optical correction. The formulation connects complex field estimation with a constrained calibration mechanism and defines the accuracy, consistency, and resource criteria needed to assess its operating range.

Keywords: Fourier Ptychography, Pupil Self Calibration, Complex Valued U Net, Aberration Estimation, Physics Constrained Reconstruction

1. Introduction

Fourier ptychographic microscopy extends the spatial bandwidth of a low numerical aperture objective by combining intensity measurements acquired under angularly varied illumination [1]. Its shifted passband acquisition scheme assembles complementary regions of the specimen spectrum into a common high resolution complex field [2]. Feature-domain backdiffraction has been developed to improve Fourier ptychographic reconstruction in the presence of vignetting and systematic errors [3]. Pupil-function-based illumination calibration estimates LED-array misalignment to improve the accuracy of the illumination geometry [4]. These developments support quantitative imaging over a large field of view, where local specimen structure must remain consistent with the angular measurement stack. The recovery problem couples several sources of uncertainty because the detector records intensity while the transmitted field contains both amplitude and phase. Overlapping Fourier measurements supply shared constraints, and their effectiveness depends on sufficient angular coverage and a consistent image formation model. Ma et al. [5] used LED-dependent temporal noise models to adapt denoising to the illumination conditions of individual Fourier ptychographic measurements. An object estimate can absorb optical mismatch, while a flexible pupil can reproduce specimen dependent residual structure.

* Corresponding author: csanad.sz@vik.bme.hu

http://dx.doi.org/10.68406/jaci.2026.vol4iss1no10:129-144

➢ This is an open access article under the CC BY-NC-SA 4.0 license (https://creativecommons.org/licenses/by/4.0/).

© Authors retain all copyrights.

This interaction complicates the interpretation of sharp features and smooth phase maps. Quantitative reconstruction consequently requires agreement across the object representation, pupil support, illumination coordinates, and detector correction. The central engineering challenge is to retain sufficient flexibility for acquisition specific aberration recovery while preserving the specimen information supported by the measured intensities.

Joint object and pupil recovery offers a direct response to this coupling by estimating the optical transfer function from the same measurements used to recover the specimen. Neural pupil engineering uses an implicit neural representation and a shifted pupil model to improve off-axis Fourier ptychographic reconstruction [6]. Aberrations vary with the optical configuration, making calibration acquired under the specimen imaging conditions particularly relevant. Joint estimation introduces additional unknowns and sensitivity to initialization, exposure imbalance, and the selected parameterization. A pupil with unrestricted spatial freedom can fit specimen dependent residuals and detector noise. Conversely, a severely restricted basis may leave genuine aberrations unmodeled. Wu et al. [7] introduced learned reconstruction methods that extract recurring specimen structure from training samples. Their computational efficiency and reconstruction fidelity depend on the correspondence between the training optical conditions and the deployed instrument. A network trained with an ideal pupil may attribute unfamiliar aberration effects to specimen texture. Training over many aberrations can increase tolerance, while acquisition specific pupil identification requires an additional calibration mechanism. The estimator must balance optical flexibility with specimen fidelity through constraints that remain interpretable across acquisition conditions and permit the influence of each parameter group to be evaluated separately. An acquisition specific correction mechanism is therefore needed if the reconstructed phase is to retain a clear physical interpretation.

Complex valued feature processing provides a natural representation for coherent fields because the real and imaginary components jointly encode amplitude and phase. Complex neural operators couple these components through structured algebra that preserves their real and imaginary interaction [8]. The resulting phase behavior depends on the nonlinearities and normalization operations used throughout the network, together with the physical constraints imposed during optimization. A U Net architecture supplies multiscale context and spatial skip connections for joint recovery of low frequency specimen structure and fine boundaries. Physics-informed neural reconstruction has also been investigated in multiplexed ptychography, where the image formation model constrains recovery from measured diffraction intensities [9]. Residual attribution remains a central challenge in separating specimen structure from optical mismatch. A strong object prior may suppress authentic specimen detail, whereas an aggressive calibration update may explain object structure through a distorted pupil. The proposed research therefore concentrates on a restricted and observable interaction between the two estimates. A complex-valued U-Net represents the object, supported phase coefficients represent the pupil, and alternating updates refine each branch against the current residual while holding the other branch fixed. This design defines a methodological hypothesis for controlled evaluation. It is intended to make calibration behavior inspectable through coefficient trajectories, held out illumination residuals, and controlled perturbation tests. The contribution considered here is the integration of constrained pupil updates with a complex object estimator and explicit diagnostics; joint object and pupil recovery itself is established prior work.

As Fourier ptychographic methods move toward quantitative use, visually plausible reconstructions require particular care because system-model mismatch can introduce errors in the recovered complex amplitude [10]. The present manuscript addresses this concern through a protocol that evaluates field accuracy and measurement consistency alongside the reconstruction formulation. The evaluation framework connects object fidelity with pupil recovery, illumination coverage, and computational cost under a common set of acquisition controls. These complementary criteria guide the comparisons and their interpretation across the selected operating conditions. The central research question concerns the ability of constrained pupil self-calibration to improve complex field estimation while preserving the separation between optical error and specimen phase. A second question concerns the conditions under which the added flexibility ceases to be identifiable, especially under reduced angular coverage or increased noise. The scientific discussion contains six sections, followed by declarations and references in Sections 7 and 8. Section 2 reviews iterative calibration, learned complex reconstruction, and the evaluation gaps connecting these approaches. Section 3 defines the forward model, the pupil constraints, and the alternating inference procedure. Section 4 describes the complex-valued U-Net, its training objective, and the intended implementation controls. Section 5 presents the benchmark protocol, reconstruction comparisons, component ablations, and sensitivity analyses across the selected operating conditions. Section 6 states the methodological contribution, its unresolved limitations, and the research directions required for experimental verification.

2. Related Work

2.1. Iterative reconstruction and optical self-calibration

Alternating projection methods recover a complex specimen by repeatedly enforcing constraints in the measurement plane and in the shared object spectrum. The overlap between adjacent spectral patches couples' exposures that would otherwise provide independent intensity observations. Joint object and pupil recovery has also been formulated using

anisotropic total variation for the object and Tikhonov regularization for the pupil [11]. The important distinction is that the pupil is shared across illumination conditions, whereas the shifted object patches change with source angle. This sharing supports optical calibration subject to the remaining object and pupil ambiguities. If the overlap is weak or the specimen lacks spectral diversity, multiple object and pupil combinations can explain nearly identical measurements. Algorithm design must therefore consider observability as well as numerical convergence. A declining residual measures agreement with the selected forward model, while factor uniqueness requires additional observability constraints.

Low dimensional aberration representations constrain pupil estimation through a basis whose coefficients have interpretable optical roles. In widefield computational adaptive optics, coordinate-based neural representations have been coupled with Zernike aberration coefficients and spatial smoothness regularization [12]. Restricting the number of coefficients reduces the opportunity to fit noise, although the chosen basis must still cover the aberrations present in the instrument. Support masks provide a complementary constraint by preventing the estimate from acquiring transfer outside the objective aperture. Illumination calibration methods address a separate geometric component of the reconstruction problem [13]. Their relevance follows from the distinct contributions of geometric and optical mismatch to the measurements. A source position error changes the sampled object spectrum, while a pupil phase error changes the coherent transfer within a sampled patch. Their residual patterns can overlap, especially near high contrast features. A credible self-calibration study should therefore control illumination geometry or evaluate its influence through an explicit sensitivity analysis.

2.2. Learned complex field reconstruction

Supervised Fourier ptychographic reconstruction maps a measurement stack or a compact initialization to a complex specimen estimate. Its learned prior reduces the computational burden of repeated phase retrieval, with generalization governed by the optical and specimen diversity represented in the training set. Neural reconstruction studies have incorporated physical image formation to connect trainable parameters with measured intensities [14]. This connection constrains learning through both an acquisition model and target image agreement. It also introduces implementation choices that affect the interpretation of performance. Training and inference must use consistent Fourier normalization, intensity scaling, cropping conventions, and boundary handling. Inconsistency in these operations can create systematic residuals that bias the object estimate.

Self-supervised complex-valued networks have been developed for wavefront phase recovery in in-line holography by combining learned representations with physical priors [15]. A complex field representation preserves continuity across phase wrapping boundaries. The selected nonlinear activations, normalization, and skip operations determine the phase dependent biases of the complex formulation. A matched two channel real network provides a controlled comparison for assessing the accuracy and computational implications of complex coupling. Residual U-Net generators have been used for complex-domain Fourier ptychographic enhancement, with encoder-decoder feature transfer through skip connections [16]. For Fourier ptychography, this multiscale feature exchange can help connect weak high frequency evidence to larger specimen structures. It can also encourage the reconstruction of familiar shapes when the measured evidence is insufficient. Measurement consistency checks, specimen separated evaluation, and inspection of difficult local regions are needed to determine the extent to which improvements reflect measurement supported information or prior dependent structure.

2.3. Coupled estimation and evaluation gaps

Unrolled and model guided networks organize learned operations around repeated applications of a physical operator. They provide an intermediate design between unconstrained image translation and fully iterative optimization. Semi-supervised Fourier ptychographic networks have combined self-supervised pupil recovery guided by Zernike modes with supervised refinement of the reconstructed image [17]. Assessment of a methodological contribution requires explicit definitions of the interaction between the estimates, the constrained ambiguities, and the evidence isolating the benefit of their coupling. The proposed design emphasizes alternating branch updates, explicit pupil gauge control, and a complex object prior evaluated against matched real valued and fixed pupil controls. These choices define the configuration and the controlled comparisons needed to assess its contribution. Relative to the two-stage strategy discussed above, the present formulation emphasizes alternating acquisition-specific coefficient refinement and object correction within one inference loop; this distinction alone does not establish superior generalization.

Evaluation practice remains a substantial source of uncertainty. Reference based accuracy depends on transparent acquisition controls, nuisance distributions, and dataset partitions. Experimental residuals assess measurement consistency, while independent phase references establish quantitative field accuracy. Cross-beamline X-ray ptychography studies have shown that probe-conditioned training can support reconstruction of previously unseen experiments [18]. For optical Fourier ptychography, relevant evaluation shifts include larger aberrations, fewer illumination angles, different photon counts, and specimen structures absent from training. Runtime comparisons additionally require equivalent hardware and a clear distinction between acquisition time, calibration time, and

reconstruction time. This manuscript uses those distinctions to organize the reconstruction evaluation. The unresolved gap is the lack of a controlled demonstration linking optical parameter recovery, complex field accuracy, and deployment cost under the same conditions. Addressing that gap requires paired numerical and physical evidence, with uncertainty evaluated using independent specimens and their grouped crop records. The discussion is weighted toward recent studies; a fuller historical account of foundational Fourier ptychography and embedded pupil recovery would improve contextual completeness.

3. Physical Formulation and Pupil Self Calibration

3.1. Coherent imaging model and supported pupil

The formulation assumes a thin specimen, spatially coherent illumination within each exposure, and a shift invariant pupil over the reconstructed patch. The specimen transmission is a complex field whose magnitude represents attenuation and whose phase represents the optical path contribution under the adopted scalar approximation. Each illumination direction shifts the specimen spectrum relative to the objective passband. The transmitted coherent field is transformed into the image plane, where the detector records its squared magnitude after exposure scaling. Background correction and detector preprocessing follow the same conventions as measurement synthesis. These relationships yield the coherent intensity equation: The forward model therefore describes a single transmitted scalar field per exposure and does not account for depth-dependent propagation within a thick scattering specimen.

$$\hat{I}_m = g_m|\mathcal{F}^{-1}\{P(\boldsymbol{k})O(\boldsymbol{k}-\boldsymbol{k}_m)\}|^2 + b_m. \tag{1}$$

In this equation, m indexes the illumination exposures, O denotes the object spectrum, $\mathbf{k}_m$ is the illumination dependent spectral displacement, and P represents the objective pupil. The Fourier transform and its inverse use matched normalization. The exposure gain g_m and background b_m are determined through calibration and held fixed during the primary comparison. Fixing these quantities limits scale ambiguity between the object and the optical model. A binary validity mask excludes saturated pixels and invalid detector responses. Evaluating predicted intensities directly on the detector grid preserves the acquisition sampling during residual calculation. The optical assumptions define the scope of the forward operator; multiple scattering, specimen motion, polarization coupling, and spatially varying aberrations require corresponding model extensions.

The pupil combines a known circular aperture support with a low dimensional phase expansion. Its magnitude remains fixed inside the aperture, defining the calibration branch as a phase aberration estimator. Eight modes excluding piston and tilt represent defocus, astigmatism, coma, trefoil, and spherical contributions under a documented basis convention. Each basis function is discretely normalized over the sampled aperture. The supported pupil equation takes the form Accordingly, pupil self-calibration in this manuscript means phase-only calibration within a prescribed aperture and basis, rather than unrestricted recovery of complex pupil transmission.

$$P(\boldsymbol{k};\boldsymbol{a}) = M(\boldsymbol{k})exp\left[i\sum_{j=1}^{8} a_j Z_j(\boldsymbol{k})\right]. \tag{2}$$

The aperture mask M and basis functions Z_j in the pupil equation are shared across illumination conditions. Their coordinate orientation matches the illumination geometry and Fourier array convention. The coefficients a_j are expressed in radians under the selected basis normalization. Excluding piston and tilt constrains common ambiguity mechanisms, while identifiability also depends on spectral coverage and specimen diversity. Registration and geometry calibration control object translation and illumination displacement. Known coefficient perturbations provide a controlled test of the direction and magnitude of the recovered optical response. Substantial transmission apodization would require a separately regularized pupil magnitude model. Mode exclusion removes selected ambiguities but does not prove uniqueness of the remaining coefficients; weak spectral overlap can still produce object-pupil tradeoffs.

3.2. Alternating object and pupil updates

Reconstruction begins with an upsampled central illumination amplitude, zero initial specimen phase, and an unaberrated supported pupil. Measurement backprojection supplies an additional complex residual feature stack to the object network. During the object step, the pupil remains fixed while the complex valued U Net predicts a bounded correction to the current field. During the pupil step, the object remains fixed while gradients of the measurement discrepancy update the aberration coefficients. Five warmup object updates provide an informative field for the first calibration gradient. The inference schedule contains ten outer cycles, with three coefficient steps in each cycle. The object step denotes refinement of the current field through the learned estimator; the stated inference schedule should not be interpreted as evidence of per-specimen network retraining.

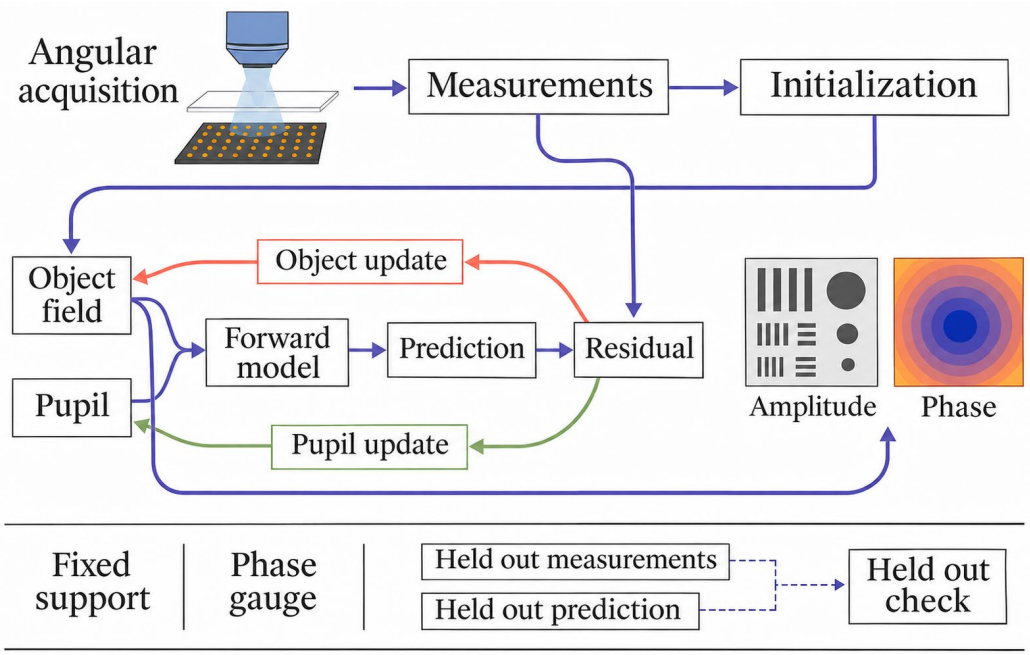


Figure 1. Workflow of acquisition specific pupil self-calibration and complex object reconstruction

Figure 1 presents the acquisition to reconstruction workflow, including detector correction, initialization, alternating updates, gauge constraints, and held out illumination checks. The same forward operator evaluates the residual after each branch update, allowing changes in measurement agreement to be associated with the active parameter group. Pupil coefficients are projected onto a bounded feasible set after each gradient step. The primary configuration limits the coefficient norm to 1.2 rad and clips coefficient gradients before projection. Every contact with the coefficient boundary is recorded because repeated saturation may indicate insufficient basis coverage or mismatch beyond the modeled aberration range. Calibration follows a projected gradient equation:

$$\boldsymbol{a}^{t+1} = \Pi_{\mathcal{A}}\left[\boldsymbol{a}^{t} - \eta_p \nabla_{\boldsymbol{a}} \mathcal{L}_{meas}\left(o^{t+1}, \boldsymbol{a}^{t}\right)\right]. \tag{3}$$

Here, $\Pi_{\mathcal{A}}$ projects the coefficient vector onto the admissible set, and η_p controls the calibration step size. The projected update equation uses the newly refined object o^{t+1} while evaluating the pupil gradient at the current coefficients. The next object step then uses the updated pupil. This ordering supports branch specific inspection of optimization behavior, with convergence dependent on initialization and local conditioning. The stopping criterion combines measurement discrepancy change with coefficient stability. The inference record retains the loss before and after each branch update, coefficient displacement, and object phase change. Multiple coefficient initializations and reversed illumination orders provide additional checks of optimization sensitivity. The ten-cycle schedule is the specified inference budget; the discrepancy and coefficient-stability criteria are convergence diagnostics unless a separate early-stopping policy is explicitly reported.

3.3. Gauge control and inference diagnostics

Global specimen phase is unobservable from the stated intensity measurements. During inference, the reconstructed field is rotated so that a selected high transmission reference region has zero circular mean phase. The reference region is fixed from the initialization and excludes pixels with very low amplitude. This operation fixes the display gauge while preserving the unobservability of absolute specimen phase. During reference-based evaluation, the estimate is additionally aligned to the known reference through a single global phase rotation. Local phase distortions are retained and contribute to the reported error. Spatial translations are determined from amplitude registration before phase comparison and reported separately under a fixed registration protocol. Neither reference-region gauge fixing nor reference-based alignment recovers absolute phase; both select a representative from intensity-equivalent solutions.

A held-out subset of illumination angles is used as an inference diagnostic. Those frames are reserved for prediction assessment, and their residual evaluates the estimated object and pupil on withheld measurements. This separation reveals cases in which a flexible pupil decreases the fitted residual while degrading prediction on other angles of the same object. For deployment evaluation, both measurement level and specimen level separation are needed. Residual maps are inspected for angular structure, edge concentration, and systematic brightfield or darkfield differences. A calibration that mainly improves brightfield exposures while worsening weak darkfield measurements may distort the recovered high frequency content even when the average discrepancy decreases. A withheld angle belongs to the same

specimen and tests angular prediction only; it cannot replace evaluation on independent parent objects or serve simultaneously as a fitted exposure.

The inference record includes the support mask, basis ordering, coefficient units, illumination coordinates, detector correction values, and normalization factors. Each item affects reproducibility and must accompany saved weights. The method also retains a fixed pupil reconstruction as a fallback diagnostic. Coefficient boundary contacts, unstable phase changes, and worsening held out consistency trigger a paired review of the calibrated and fixed pupil outputs. Such diagnostics define the limits of the reconstruction claim. They provide evidence about numerical consistency, while independently calibrated measurements are still required to establish optical accuracy.

4. Complex Valued U Net and Optimization Design

4.1. Coupled feature processing and multiscale architecture

The object branch contains four encoder levels with complex feature widths of 24,48,96, and 192. Each level uses two coupled convolution blocks, followed by downsampling between successive resolutions. The decoder restores spatial resolution through interpolation and complex convolution. Skip connections concatenate encoder and decoder features at matching resolutions along the complex channel dimension. The network receives the current complex field, a complex backprojected measurement residual, and a real confidence map embedded as a complex channel with zero imaginary component. These inputs condition the estimator on both the current reconstruction and acquisition specific disagreement. The output is a complex residual multiplied by a learned scalar gate constrained between zero and one, then added to the current object estimate.

Complex convolution couples real and imaginary feature components through paired kernels. Writing $W = W_r + iW_i$ and $z = z_r + iz_i$, the convolution equation is

$$W * z = (W_r * z_r - W_i * z_i) + i(W_r * z_i + W_i * z_r). \tag{4}$$

The coupling in this equation preserves complex multiplication within the linear operation. Split nonlinearities act separately on real and imaginary components, yielding a nonholomorphic network. The architectural comparison therefore concerns the structured coupling of coherent features and its interaction with the selected nonlinear operations. A matched real two-channel U-Net provides the corresponding control. Feature capacity or computational cost must be matched according to a declared comparison policy so that parameter count remains distinguishable from the effect of complex representation. In particular, split nonlinearities do not generally commute with arbitrary global phase rotations, so exact phase equivariance of the complete network is not claimed.

The implementation uses split leaky rectification and shared spatial dropout masks for paired feature components. Normalization constrains independent rescaling of real and imaginary outputs at the reconstruction head. The final layer directly predicts the two components of the complex field, from which amplitude and phase are calculated for evaluation and display. Figure 2 details the encoder-decoder, residual input path, shared optical operator, and pupil calibration loop. Solid arrows represent feature transport, while curved arrows indicate alternating optimization feedback. The architecture diagram identifies the active and frozen parameter groups during each update.

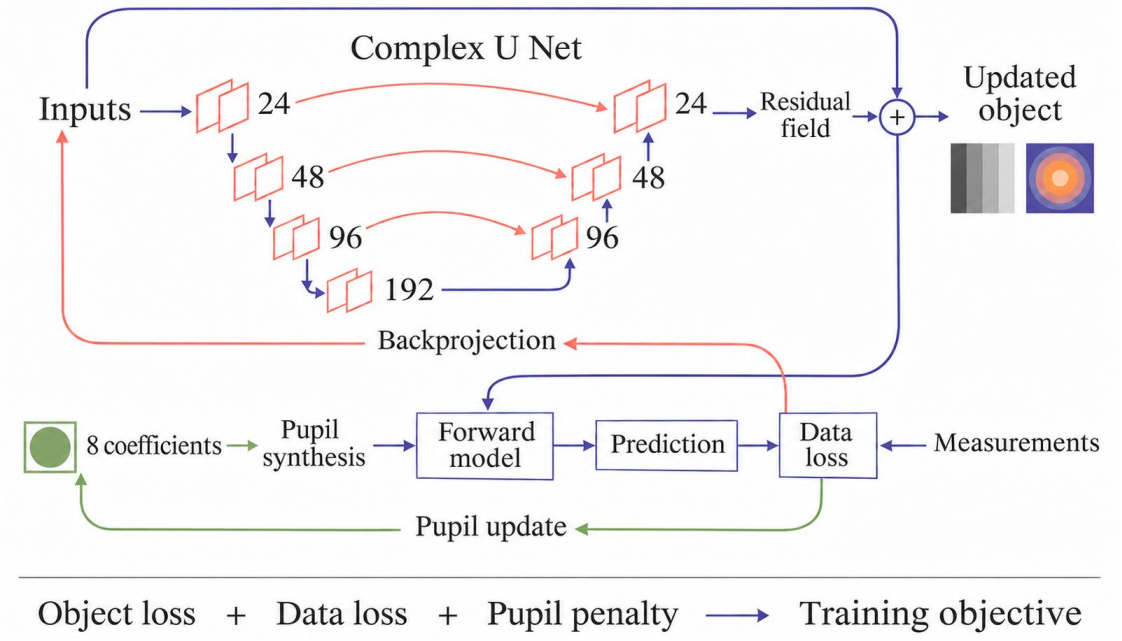


Figure 2. Architecture and alternating optimization of the complex valued U Net

4.2. Training objective and optimization schedule

The training objective combines an exposure balanced amplitude discrepancy, supervised complex field agreement, and pupil coefficient regularization. Amplitude comparison reduces the dominance of high intensity frames in the measurement term. A small positive offset stabilizes the square root near the detector background level. Exposure weights follow a fixed calibration rule throughout pupil optimization. The supervised term compares globally aligned complex fields, preserving their coupled amplitude and phase representation across phase wrapping boundaries. These components enter the objective equation as

$$\mathcal{L} = \lambda_m \mathcal{L}_{meas} + \lambda_o \mathcal{L}_{object} + \lambda_a \|\boldsymbol{a}\|_2^2. \tag{5}$$

The weights in the objective equation are initially set to 1.0 for measurement consistency, 0.2 for object supervision, and 0.001 for coefficient regularization. Their effective contributions depend on the normalization of the constituent losses. Each data discrepancy is therefore averaged over valid pixels and available measurements before weighting. Explicit reduction conventions make the loss configuration reproducible across different acquisition layouts. Training uses specimen separated mini batches, with every crop from a parent object assigned to the same partition. Aberrations are sampled independently of object identity to limit associations between specimen morphology and pupil coefficients. Illumination count varies within the supported layouts, and an availability map identifies missing exposures. The numerical coefficient penalty is meaningful only together with the stated loss reductions and basis normalization; it is not a dimension-independent setting transferable unchanged between implementations.

The measurement discrepancy compares predicted and observed amplitudes over valid detector pixels. Calibration based normalization accounts for exposure scale before evaluating the loss. Averaging over available frames keeps its magnitude comparable across illumination subsets. Under strongly signal dependent noise, a likelihood matched discrepancy provides an additional comparison. The noise sensitivity analysis examines the operating range of the selected amplitude criterion. With the exposure scales already incorporated into the normalized measurements, the measurement loss equation becomes

$$\mathcal{L}_{meas} = \frac{1}{N} \sum_{m=1}^{N} \frac{\left\| V_m \odot \left(\sqrt{\hat{I}_m + \varepsilon} - \sqrt{I_m + \varepsilon} \right) \right\|_2^2}{n_m}. \tag{6}$$

In the measurement loss equation, N denotes the number of available frames, V_m is the binary validity mask, and n_m is its valid pixel count. The offset ε equals one millionth of the normalized peak intensity, and $\odot$ denotes elementwise multiplication. Optimization uses Adam with an initial object learning rate of 0.0002, a coefficient learning rate of 0.001, and cosine decay over 150 epochs. Checkpoint selection minimizes validation complex field error subject to acceptable held out measurement consistency. Convergence records, optimizer states, and the random seeds governing training perturbations form part of the reproducibility record.

4.3. Implementation controls and computational reporting

The implementation uses single precision complex tensors for Fourier operations and paired real tensors for coupled convolutions. Coefficient gradient verification uses single precision arithmetic because small pupil phase updates can be sensitive to rounding. Synthesis and backprojection share the same padding, cropping, and Fourier normalization conventions. A numerical adjoint check verifies the linear field propagation operator before application of the intensity nonlinearity. Finite difference checks of selected aberration coefficients independently assess the calibration gradient. These checks establish operator consistency, while reconstruction accuracy is evaluated against reference fields. A reproducible finite-difference check additionally requires the perturbation size, a step-size sweep, and a relative-error tolerance; without these records, operator consistency cannot be independently confirmed from this description.

Computational reporting separates network initialization, iterative refinement, and optional validation passes. The timing values in the following section describe reconstruction of a single field after model loading. Acquisition, training, disk transfer, and instrument synchronization are recorded as separate operations. All methods use the same accelerator, numerical precision, and device synchronization procedure. At least one warmup reconstruction precedes timing, and repeated synchronized runs provide the median duration. Peak memory is measured over the complete inference sequence, including intermediate Fourier buffers. Measurement stacks and retained iterative states contribute to memory allocation alongside the network parameters.

Model selection first considers aligned phase accuracy and amplitude fidelity, followed by held out consistency, calibration stability, and computational cost. Inspection of coefficient boundary contacts supports interpretation of reductions in the fitted residual. Sensitivity tests vary the coefficient bound, warmup duration, and number of calibration

cycles under a common validation protocol. The reproducibility package includes operator tests, optical metadata, configuration files, trained checkpoints, and specimen split identifiers. Together, these materials specify the acquisition assumptions, numerical conventions, and optimization settings governing the reconstruction procedure.

5. Experimental Evaluation and Reconstruction Analysis

5.1. Benchmark protocol and reconstruction fidelity

Defocus estimation has been shown to improve digital refocusing in Fourier ptychographic microscopy [19]. The evaluation protocol compares reconstruction accuracy under matched acquisition and optical settings so that model mismatch remains distinguishable from differences between estimators. The benchmark contains 1,000 training objects, 100 validation objects, and 200 test objects on a 512 by 512 grid, with parent identities separated across partitions. Table 1 specifies a wavelength of 532 nm, objective numerical aperture of 0.10, illumination numerical aperture of 0.40, 121 primary exposures, pupil phase root mean square of 0.30 rad, and normalized intensity noise standard deviation of 0.01. Figure 3(a) compares amplitude scores of 27.6, 30.4, 29.8, 31.2, and 34.8 dB for AP, EPRY, Real U Net, Complex U Net, and Proposed, respectively. The calibrated complex configuration exceeds the fixed pupil complex configuration by 3.6 dB, corresponding to an amplitude mean squared error ratio of approximately 0.44 under a shared reference range. That contrast isolates the calibration contribution more directly than comparison with the structurally different iterative methods. The 32 dB line defines an evaluation target. Reference normalization remains fixed across methods to preserve the comparability of amplitude scores. The stated benchmark scores should be interpreted within the specified reference-based comparison; the description does not establish independent physical-instrument validation or document the provenance of every underlying object.

Table 1. Benchmark configuration and evaluation controls

Setting	Proposed value	Control
Object grid	512 × 512	Shared by methods
Objects train / val / test	1000 / 100 / 200	Parent identity separated
Wavelength	532 nm	Coherent forward model
Objective / illumination NA	0.10 / 0.40	Fixed geometry
Primary frame count	121	Known source positions
Pupil phase RMS	0.30 rad	Basis matched primary case
Intensity noise SD	0.01	Normalized intensity units
Pupil phase modes	8	No piston or tilt
Training epochs	150	Optimizer schedule
Outer calibration cycles	10	Three pupil steps per cycle

Global phase gauge alignment is required for meaningful comparison of coherent fields recovered from intensity measurements [20]. The evaluation applies amplitude-based registration followed by one global phase rotation, and retains pixels whose reference amplitude exceeds 0.10. Figure 3(b) gives phase errors of 0.310, 0.220, 0.245, 0.187, and 0.118 rad in the same method order. The 0.069 rad reduction between the fixed pupil complex and calibrated complex configurations corresponds to 36.9 percent of the former error. Agreement between this phase ordering and the amplitude ordering is relevant because attenuation contrast and optical path accuracy reflect different aspects of the recovered field. The proposed configuration also lies 0.032 rad below the provisional 0.15 rad phase target, whereas the fixed pupil complex configuration exceeds it by 0.037 rad. These margins depend on the evaluation mask: including near zero amplitude pixels would place greater weight on poorly defined phase values. The mask is therefore determined from the reference and reused unchanged for every method. The evaluation record should retain registration displacements and report sensitivity to the amplitude cutoff so that spatial alignment and phase masking remain visible components of the evaluation protocol. The 32 dB and 0.15 rad thresholds are provisional comparison targets, not validated clinical or metrological acceptance limits.

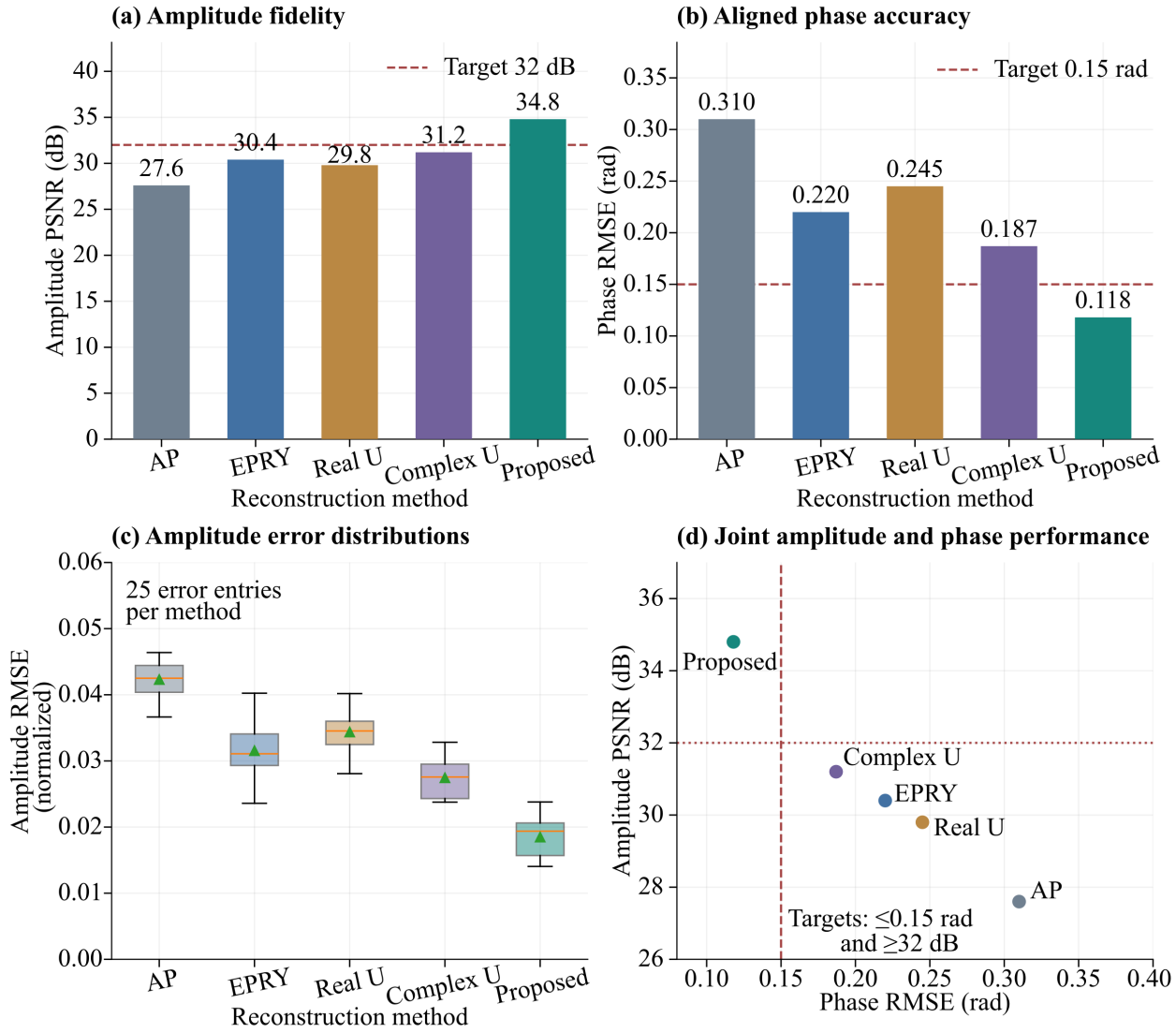


Figure 3. Reconstruction fidelity across five configurations. (a) Amplitude peak signal to noise ratio with a 32 dB target. (b) Aligned phase root mean square error with a 0.15 rad target. (c) Amplitude error distributions with 25 error entries per method. (d) Phase error versus amplitude fidelity with method labels

Figure 3(c) examines amplitude error distributions using 25 entries per configuration. The distribution centers are 0.042, 0.031, 0.035, 0.027, and 0.018 in normalized amplitude units, with a common reference dispersion of 0.003. The 0.009 separation between the final two centers places the calibration contrast against an explicit within configuration spread. The boxes display medians, quartiles, extrema under the selected whisker convention, and mean markers; each element describes a different aspect of the error distribution. Their joint interpretation separates central accuracy from variability and tail behavior across the comparison configurations. Structural similarity depends on the chosen kernel and implementation, and averaging local scores can obscure localized reconstruction errors [21]. Table 2 therefore pairs amplitude and phase metrics with structural similarity values of 0.872, 0.918, 0.905, 0.932, and 0.961. The 0.029 increase between the final two configurations accompanies the lower amplitude error center, which is consistent with the intended preservation of local contrast. Validation should inspect textured and weakly absorbing regions separately because a strong average structural score can coexist with localized phase distortion. Every crop from one parent object remains within the same dataset partition and contributes to that parent's aggregate evaluation record. The 25 displayed entries and common reference dispersion do not document the full 200-object test distribution; selection and aggregation records are needed before interpreting them as population variability.

Table 2. Reconstruction fidelity, pupil recovery error, and inference cost across five configurations

Method	PSNR dB	SSIM	Phase rad	Pupil rad	Time s	Memory GB
AP	27.6	0.872	0.310	0.241	8.4	1.8
EPRY	30.4	0.918	0.220	0.126	12.7	2.0

Real U Net	29.8	0.905	0.245	0.241	0.09	2.1
Complex U Net	31.2	0.932	0.187	0.241	0.11	2.4
Proposed	34.8	0.961	0.118	0.072	0.42	3.1

Figure 3(d) locates each method jointly in phase error and amplitude fidelity space. The calibrated configuration occupies the region satisfying both provisional thresholds; the other configurations occupy regions that exceed the phase limit, fall below the amplitude target, or both. This geometry makes the acceptance criterion explicit and permits disagreement between the metrics to remain visible. Table 2 adds pupil errors of 0.241, 0.126, 0.241, 0.241, and 0.072 rad, reconstruction times of 8.4, 12.7, 0.09, 0.11, and 0.42 s, and peak memory values of 1.8, 2.0, 2.1, 2.4, and 3.1 GB. The fixed pupil entries quantify discrepancy from the ideal pupil retained by those methods. GPU performance studies use warmup runs and repeated kernel timings to characterize execution cost [22]. Runtime reporting should additionally specify device synchronization and the warmup procedure used for each implementation. Under the comparison values, calibration adds 0.31 s and 0.7 GB relative to the direct complex estimator. The suitability of this computational cost depends on the application latency limit and quantitative phase accuracy requirements. A deployment comparison should retain separate acquisition, initialization, refinement, and validation durations, since repeated calibration on a stable instrument may distribute its cost differently from calibration performed for every field.

5.2. Aberration tolerance and calibration behavior

Zernike modal analysis has been used to examine the recovered wavefront in digital-refocusing Fourier ptychography [23]. The aberration stress evaluation uses basis matched pupil perturbations at 0.00, 0.10, 0.20, 0.30, 0.40, and 0.50 rad root mean square, with specimen identity and noise realization paired across levels. Figure 4(a) reports the proposed configuration phase errors of 0.082, 0.089, 0.101, 0.118, 0.145, and 0.183 rad. At the largest perturbation, the corresponding fixed pupil complex and iterative configurations reach 0.310 and 0.340 rad. The proposed curve crosses the provisional 0.15 rad target between the final two stress levels, while the fixed pupil complex curve reaches that target at 0.20 rad. The increase from 0.30 to 0.50 rad is 0.065 rad for the calibrated configuration, compared with 0.123 rad for the fixed pupil configuration. This increasing sensitivity is compatible with stronger coupling between object detail and aberration compensation at larger perturbations. Further sensitivity tests should vary coefficient composition at each stress level, because a common wavefront norm can represent different distributions of defocus, astigmatism, and coma. Grouping results by aberration family would reveal whether aberration tolerance depends on the modal composition represented in the training distribution. These stress results concern basis-matched phase aberrations and do not establish tolerance to illumination misalignment, amplitude apodization, or aberrations outside the selected expansion.

Figure 4(b) compares eight injected coefficients of 0.18, -0.12, 0.09, 0.06, -0.08, 0.05, 0.10, and -0.04 rad with recovered coefficient values of 0.17, -0.11, 0.085, 0.055, -0.073, 0.047, 0.093, and -0.035 rad. These coefficients describe a separate diagnostic pupil. Their root mean squared coefficient discrepancy is approximately 0.0069 rad under the stated basis normalization. Every recovered coefficient preserves the injected sign, while its magnitude is slightly smaller. The pattern is compatible with regularization toward the initial pupil and provides a specific bias to examine during implementation. The identity line allows sign reversal and proportional shrinkage to be distinguished visually. Mode wise absolute differences range from 0.003 to 0.010 rad, with the largest discrepancies assigned to the two largest injected magnitudes. Machine-learning benchmark studies have used capacity-matched, jointly tuned ablations to separate the effect of an attention mechanism from model size and hyperparameter budget [24]. A calibration study should therefore retain the same basis and support while varying the update schedule or coefficient penalty. Recovered coefficient accuracy should be interpreted jointly with the object field because a coefficient vector can approach its target while the specimen estimate retains spatially structured error. For an orthonormal sampled basis, the pupil phase RMS equals the coefficient error Euclidean norm, whereas the coefficient RMS divides that norm by the square root of eight; the two quantities must not be interchanged.

Figure 4(c) follows the same eight diagnostic coefficients through ten calibration cycles. The coefficient trajectory reaches approximately 36.5 percent of its terminal coefficient vector after the first cycle, 89.7 percent after the fifth, and 98.9 percent after the tenth. The heatmap displays an approach to a stable pupil with diminishing update magnitude. This pattern can be assessed alongside branch specific discrepancy changes, coefficient reversals, and contacts with the allowed coefficient boundary. Relative coefficient changes complement the shared color scale by revealing substantial proportional updates in small magnitude modes. The saved coefficient array therefore accompanies the figure. During inference, the branch specific loss change should be logged beside coefficient displacement, with illumination order and optimizer state held fixed during schedule comparisons. A rapid coefficient change accompanied by rising held out discrepancy would indicate divergence between fitting accuracy and predictive consistency. A slowly changing coefficient vector accompanied by persistent angular residuals would motivate inspection of the basis, geometry, and gain calibration. These alternatives link observable trajectory patterns to specific components of the forward model that can be examined separately.

Figure 4(d) displays empirical cumulative phase error distributions for five configurations, each represented by 40 error entries. The distribution centers follow the primary phase values of 0.310, 0.220, 0.245, 0.187, and 0.118 rad, with a common reference dispersion of 0.025 rad. The leftward position of the calibrated configuration describes lower errors across most of its distribution, whereas the tails indicate the spread of the corresponding error entries. The 0.15 rad line makes the fraction meeting the provisional criterion directly inspectable. Bootstrap studies of hierarchical data emphasize preserving dependencies between grouping levels during resampling [25]. Confidence interval estimation should therefore operate on independent parent object outcomes, with every method evaluated on the same parents. The number of distribution entries and the size of the complete test partition should be recorded separately. Distribution width should also be stratified by reference phase range and spectral content. Broad tails concentrated among weakly transmitting specimens would motivate amplitude aware loss weighting; tails concentrated among specimens with strongly directional structure would motivate examination of angular coverage and pupil observability. The 40-entry curves are descriptive summaries; neither statistical significance nor confidence interval coverage follows from their ordering without parent-level records and a specified sampling procedure.

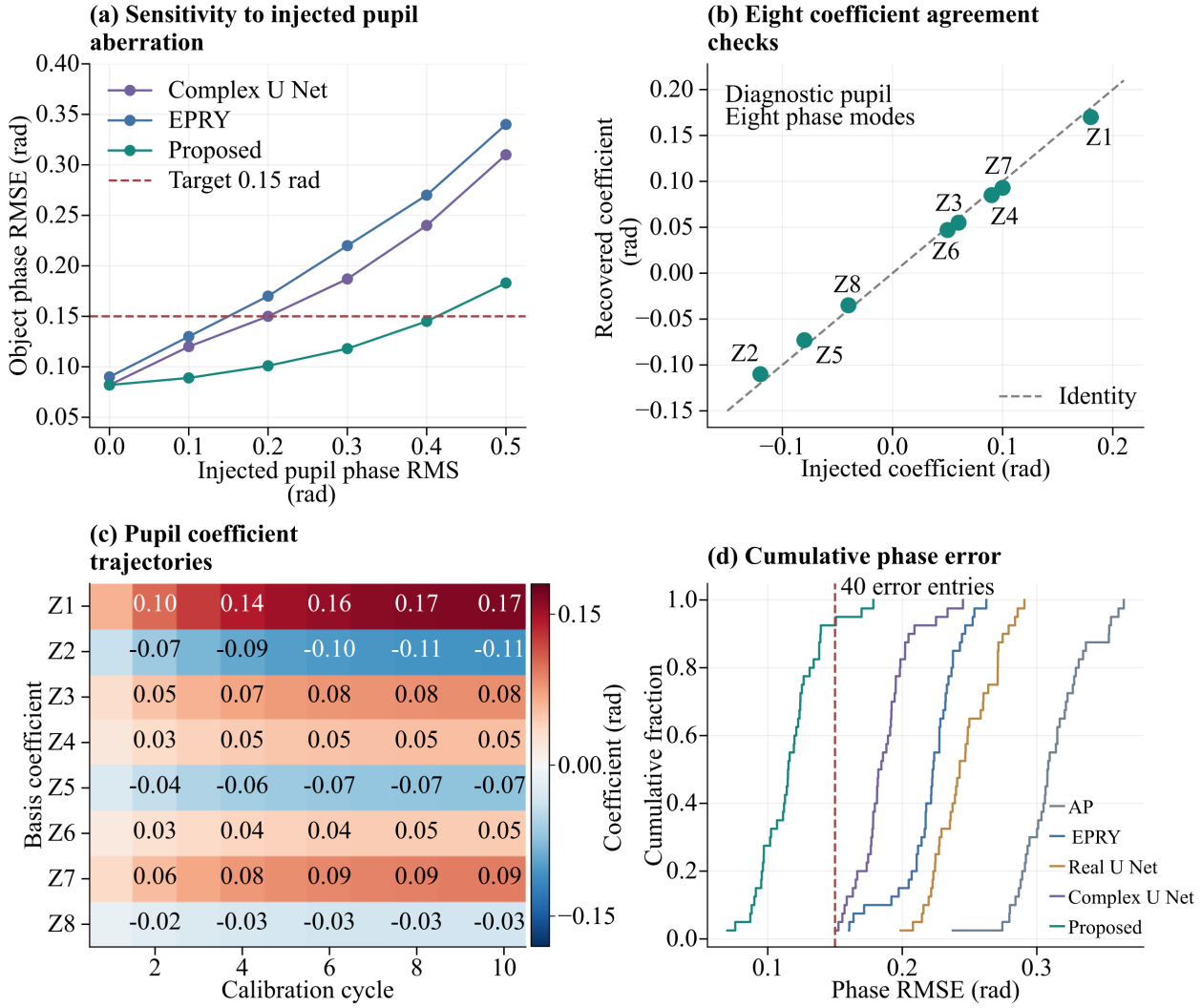


Figure 4. Pupil calibration diagnostics. (a) Phase error versus six aberration levels for three methods. (b) Injected and recovered values for eight coefficients in a separate diagnostic case. (c) Eight coefficient trajectories over ten calibration cycles. (d) Empirical cumulative phase error distributions for five methods

5.3. Component attribution and operating sensitivity

Figure 5(a) compares amplitude scores of 31.2, 32.4, 30.6, 33.1, and 34.8 dB for No Calibration, Real Features, No Measurement Loss, Joint Update, and Full Model. The 2.4 dB gap between Real Features and Full Model defines the intended test of coupled complex processing under a shared calibration schedule. The 4.2 dB gap associated with removing the training measurement term is larger, suggesting that physical consistency deserves separate examination from feature representation under this evaluation protocol. The No Measurement Loss configuration retains supervised object training and the measurement-based pupil update at inference. Figure 5(b) gives corresponding phase errors of 0.187, 0.162, 0.214, 0.149, and 0.118 rad. The 0.031 rad difference between Joint Update and Full Model accompanies a 1.7 dB amplitude difference, providing a paired accuracy contrast for the optimization schedule. The comparison

requires learning rate retuning within the same validation budget, since a schedule can appear inferior when its step sizes favor another update policy. Saved branch gradients and per cycle discrepancy changes would help distinguish gradient interference from differences in convergence speed. Model capacity, illumination frames, and the total number of forward operator evaluations remain controlled during this attribution test. Thus, this ablation removes the training measurement term only; it is not an inference configuration without physical measurement information.

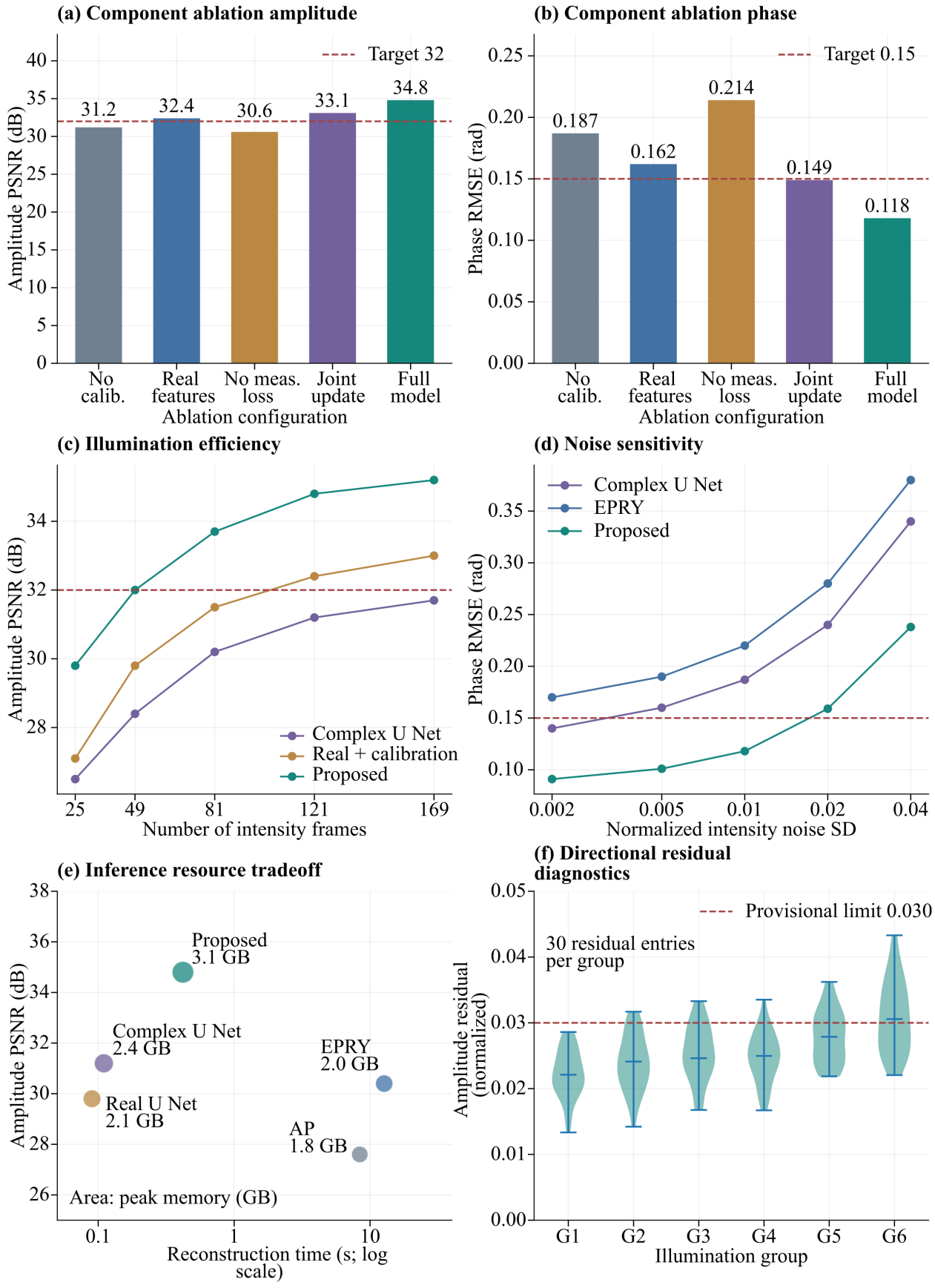


Figure 5. Ablation and resource tradeoffs. (a) Amplitude fidelity for five ablations. (b) Phase error for the same ablations. (c) Fidelity versus five frame counts for three methods. (d) Phase error versus five noise levels for three methods. (e) Runtime versus fidelity for five methods with memory scaled markers. (f) Residual distributions across six illumination groups

Hyperuniform illumination subsampling has been investigated to reduce the number of exposures while preserving reconstruction quality and high-frequency information in Fourier ptychographic microscopy [26]. Figure 5(c) reports the proposed configuration amplitude scores of 29.8, 32.0, 33.7, 34.8, and 35.2 dB for 25, 49, 81, 121, and 169 frames. The initial increase of 2.2 dB over 24 added exposures is larger than the final increase of 0.4 dB over 48 exposures. The corresponding marginal gains are approximately 0.092 and 0.008 dB per frame under the specified layouts. These values identify an acquisition efficiency contrast that should be tested with equal photon budgets and published illumination coordinates. Figure 5(d) reports phase errors of 0.091, 0.101, 0.118, 0.159, and 0.238 rad as normalized intensity noise standard deviation increases through 0.002, 0.005, 0.010, 0.020, and 0.040. Fourier ptychographic denoising studies distinguish signal-dependent noise from signal-independent noise and use darkfield measurements to characterize the latter component [27]. Under the additive noise condition, the phase target is crossed between noise levels of 0.010 and 0.020. Increasing phase error at the upper levels motivates examination of exposure weighting and darkfield residuals, where low signal measurements may become particularly influential after normalization. Because exposure number alone does not fix total photon dose or acquisition duration, the frame-count curve does not by itself establish dose efficiency or a measured acquisition-speed improvement.

Figure 5(e) relates runtime to amplitude fidelity while marker area encodes peak memory. The proposed configuration occupies 0.42 s and 3.1 GB, compared with 0.11 s and 2.4 GB for Complex U Net. It therefore assigns a 3.82-fold latency factor and a 29.2 percent memory increase to the calibrated configuration. Relative to the 12.7 s iterative joint recovery configuration, the same proposed value represents a much shorter refinement interval under the specified timing convention. Device precision, synchronization, and forward evaluation counts must accompany runtime records. Figure 5(f) examines directional residual distributions across six illumination groups, each with 30 residual entries. Their distribution centers rise from 0.022 to 0.030 normalized amplitude units, placing the final group at the provisional residual limit. A directional gradient of this form would warrant inspection of source brightness correction, pupil orientation, and asymmetric spectral coverage during acquisition analysis. Quantitative phase microscopy has used targets with manufacturer-specified atomic force microscopy measurements to calibrate phase-derived height estimates [28]. Such reference measurements would help determine whether a directional residual pattern corresponds to an optical bias or to limitations of the thin specimen model. Group specific raw exposures and corrected residuals should be retained together for that comparison. The 0.42 s figure describes the stated post-loading reconstruction interval only; without the accelerator model and complete timing records, it is not a reproducible end-to-end instrument latency.

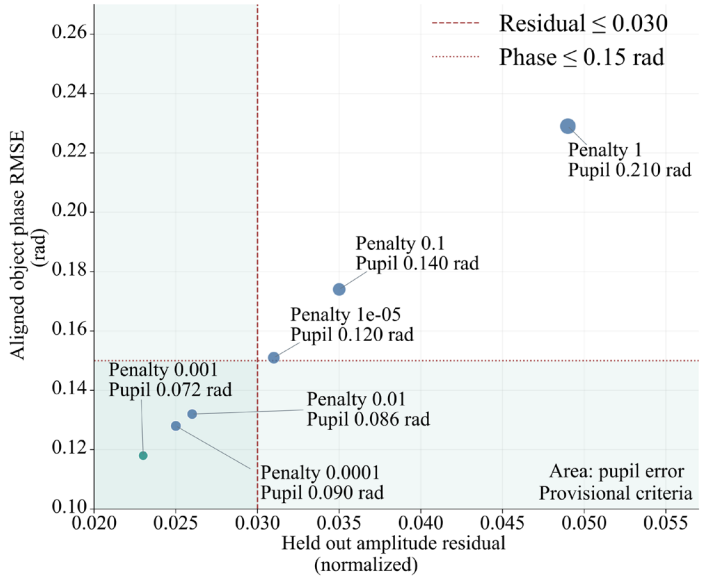


Figure 6. Regularization sensitivity

Figure 6 examines six pupil penalty weights of 0.00001, 0.0001, 0.001, 0.01, 0.1, and 1.0. Their phase errors are 0.151, 0.128, 0.118, 0.132, 0.174, and 0.229 rad, while held out amplitude residuals are 0.031, 0.025, 0.023, 0.026, 0.035, and 0.049. The intermediate weight of 0.001 gives the lowest value of both quantities and a pupil error of 0.072 rad. Reducing the penalty weight to 0.00001 increases phase error by 0.033 rad, consistent with greater coefficient freedom; increasing it to 1.0 raises phase error by 0.111 rad, consistent with stronger shrinkage toward the initial pupil. The two neighboring weights also satisfy the displayed acceptance criteria, defining a provisional operating interval

around the selected setting. The residual margin is 0.007 at the central weight, compared with 0.005 and 0.004 at the neighboring settings. These margins quantify the tolerance to residual variation across repeated acquisitions near the acceptance threshold. Validation should track this interval across aberration families and specimen transmission ranges, with the test partition reserved for the fixed configuration. A shift of the interval toward weaker penalties for high aberration cases would motivate scaling the regularizer with a calibrated optical prior; a shift associated mainly with exposure noise would motivate revisiting the discrepancy weighting. The numerical distances from the threshold are descriptive margins, not empirically established tolerances to repeated-acquisition variation.

6. Conclusion

This manuscript formulated a Fourier ptychographic reconstruction method that integrates a complex-valued U-Net with constrained pupil self-calibration. The object branch represents the coherent specimen field, while a supported aberration basis describes acquisition specific pupil phase. Alternating updates and explicit gauge conventions make the interaction between object refinement and optical correction inspectable. The accompanying benchmark design connects reconstruction fidelity with coefficient recovery, measurement consistency, ablation controls, and computational cost. The evaluation framework connects the recovered field with optical parameter behavior and operating constraints across the selected comparisons.

The present formulation has several limitations. Its optical model assumes a thin specimen and a shift invariant, phase only pupil. A restricted aberration basis covers a finite class of transfer errors, while alternating optimization remains subject to the nonuniqueness of joint object and pupil estimation. Learned specimen priors may also distort unfamiliar structures when the measurement evidence is weak. The reliability of the learned prior also depends on specimen diversity, exposure balance, and the accuracy of the acquisition geometry used during inference. The most plausible application is patchwise imaging of thin, approximately stationary specimens with calibrated illumination; thick scattering samples and whole-field spatial variation require additional modeling and independent validation.

Future work should extend operator verification and evaluate specimen separated datasets across a broader range of optical conditions. Independent phase targets and pupil measurements would help separate genuine instrument recovery from compensation for object bias. Extensions should examine spatially varying pupils, partial coherence, and noise models matched to the detector. Adaptive illumination selection may improve acquisition efficiency if it preserves identifiability. Releasing code, calibration metadata, split definitions, and failure cases would make subsequent comparisons more informative and support a reproducible assessment of the proposed reconstruction strategy.

7. Declarations

7.1 Author Contributions

Szűcs Csanád contributes to conceptualization, methodology, software, validation, analysis, investigation, data collection, draft preparation, manuscript editing, visualization, supervision, project administration, and funding acquisition. Horváth Zsuzsanna contributes to validation, analysis, investigation, data collection, draft preparation. All authors have read and agreed with the manuscript before its submission and publication.

7.2 Funding and Acknowledgments

This research received no specific financial support from any funding agency.

7.3 Institutional Review Board Statement

Not applicable.

7.4 Informed Consent Statement

Not applicable.

7.5 Date Availability

Not applicable.

7.6 Declaration of Competing Interest

The authors declare that they have no known competing financial interests or personal relationships that could have appeared to influence the work reported in this paper.

7.7 Declaration of generative AI and AI-assisted technologies

During the preparation of this manuscript, the authors utilized Quillbot for linguistic polishing, logical organization and draft revision. The generative AI tool was not involved in research design, data collection, data analysis, or the equation of core conclusions. All outputs generated by AI were reviewed, revised and verified manually by the authors. The authors take full responsibility for all content of this manuscript.

8. References

[1] Eadie, F., Copeland, L., Di Caprio, G., McConnell, G., & Kallepalli, A. (2025). Fourier ptychography microscopy for digital pathology. Journal of Microscopy, 300(2), 260–285. https://doi.org/10.1111/jmi.70001

[2] Shu, Y., Sun, J., Fan, Y., Jin, Y., Chen, Q., & Zuo, C. (2024). Diagonal illumination scheme for Fourier ptychographic microscopy: Resolution doubling and aliasing minimization. Journal of the Optical Society of America A, 41(11), C62–C71. https://doi.org/10.1364/josaa.532252

[3] Zhang, S., Wang, A., Xu, J., Feng, T., Zhou, J., & Pan, A. (2024). FPM-WSI: Fourier ptychographic whole slide imaging via feature-domain backdiffraction. Optica, 11(5), 634–646. https://doi.org/10.1364/optica.517277

[4] Liu, H., Xu, T., Chen, Y., Wang, Y., & Li, J. (2024). Transformed pupil-function misalignment calibration strategy for Fourier ptychographic microscopy. Optics Express, 32(7), 11429–11446. https://doi.org/10.1364/oe.515196

[5] Ma, Q., Zhao, J., & Cui, G. (2024). LED-based temporal variant noise model for Fourier ptychographic microscopy. Optics Express, 32(8), 14620–14644. https://doi.org/10.1364/oe.518908

[6] Zhang, S., & Cao, L. (2025). Whole-field, high-resolution Fourier ptychography with neural pupil engineering. Optica, 12(10), 1615–1624. https://doi.org/10.1364/optica.575065

[7] Wu, K., Pan, A., & Gao, W. (2024). Fourier ptychographic reconstruction with denoising diffusion probabilistic models. Optics & Laser Technology, 176, Article 111016. https://doi.org/10.1016/j.optlastec.2024.111016

[8] Costanzo, S., & Flores, A. M. (2025). From iterative methods to neural networks: Complex-valued approaches in medical image reconstruction. Electronics, 14(10), Article 1959. https://doi.org/10.3390/electronics14101959

[9] Wengrowicz, O., Bronstein, A. M., & Cohen, O. (2024). Unsupervised physics-informed deep learning-based reconstruction for time-resolved imaging by multiplexed ptychography. Optics Express, 32(6), 8791–8803. https://doi.org/10.1364/oe.515445

[10] Yin, T., Song, G., Lee, D., Oh, J., & Jang, M. (2025). Impact of system-model mismatch in Fourier ptychographic microscopy. Advanced Photonics Research, 6(12), Article e202500180. https://doi.org/10.1002/adpr.202500180

[11] Lee, K. C., Chae, H., Xu, S., Lee, K., Horstmeyer, R., Lee, S. A., & Hong, B.-W. (2024). Anisotropic regularization for sparsely sampled and noise-robust Fourier ptychography. Optics Express, 32(14), 25343–25361. https://doi.org/10.1364/oe.529023

[12] Kang, I., Zhang, Q., Yu, S. X., & Ji, N. (2024). Coordinate-based neural representations for computational adaptive optics in widefield microscopy. Nature Machine Intelligence, 6(6), 714–725. https://doi.org/10.1038/s42256-024-00853-3

[13] Arcab, P., Rogalski, M., Trusiak, M., & Zdańkowski, P. (2025). Two-step automated method for robust Fourier ptychographic microscopy LED misalignment calibration. Optics and Lasers in Engineering, 195, Article 109340. https://doi.org/10.1016/j.optlaseng.2025.109340

[14] Chen, Q., Cai, C.-T., He, X.-T., & Chen, R. (2025). Fourier ptychographic microscopy with a two-stage physics-enhanced neural network. Optics & Laser Technology, 181, Article 112016. https://doi.org/10.1016/j.optlastec.2024.112016

[15] Dou, J., An, Q., Liu, X., Mai, Y., Zhong, L., Di, J., & Qin, Y. (2025). Enhanced phase recovery in in-line holography with self-supervised complex-valued neural networks. Optics and Lasers in Engineering, 184, Article 108685. https://doi.org/10.1016/j.optlaseng.2024.108685

[16] Bardozzo, F., Fiore, P., Valentino, M., Bianco, V., Memmolo, P., Miccio, L., Brancato, V., Smaldone, G., Gambacorta, M., Salvatore, M., Ferraro, P., & Tagliaferri, R. (2024). Enhanced tissue slide imaging in the complex domain via cross-explainable GAN for Fourier ptychographic microscopy. Computers in Biology and Medicine, 179, Article 108861. https://doi.org/10.1016/j.compbiomed.2024.108861

[17] Zhou, X., Tong, H., Ouyang, E., Zhao, L., & Fang, H. (2025). Fourier ptychographic microscopy with optical aberration correction and phase unwrapping based on semi-supervised learning. Applied Sciences, 15(1), Article 423. https://doi.org/10.3390/app15010423

[18] Vong, A., Henke, S., Hoidn, O., Ruth, H., Deng, J., Hexemer, A., Shapiro, D., Mehta, A., Gleason, A., Hancock, L., & Schwarz, N. (2026). Towards generalizable deep ptychography neural networks. npj Computational Materials, 12, Article 368. https://doi.org/10.1038/s41524-026-02198-4

[19] Liu, M., Wu, R., Luo, Z., Zhen, J., Zhang, H., Luo, J., Yan, L., & Wu, Y. (2024). Fast digital refocusing Fourier ptychographic microscopy method based on convolutional neural network. Optics Express, 32(1), 339–354. https://doi.org/10.1364/oe.512330

[20] Allain, M., Aslan, S., Coene, W., Dirksen, S., Dong, J., Flamant, J., Iwen, M., Krahmer, F., van Leeuwen, T., Melnyk, O., Menzel, A., Mosk, A. P., Nikitin, V., Salanevich, P., Plonka, G., & Wellershoff, M. (2025). Phasebook: A survey of selected open problems in phase retrieval. Sampling Theory, Signal Processing, and Data Analysis, 23(2), Article 23. https://doi.org/10.1007/s43670-025-00117-0

[21] Breger, A., Biguri, A., Landman, M. S., Selby, I., Amberg, N., Brunner, E., Gröhl, J., Hatamikia, S., Karner, C., Ning, L., Dittmer, S., Roberts, M., AIX-COVNET Collaboration, & Schönlieb, C.-B. (2025). A study of why we need to reassess full reference image quality assessment with medical images. Journal of Imaging Informatics in Medicine, 38(6), 3444–3469. https://doi.org/10.1007/s10278-025-01462-1

[22] Pekkilä, J., Lappi, O., Robertsén, F., & Korpi-Lagg, M. J. (2025). Stencil computations on AMD and Nvidia graphics processors: Performance and tuning strategies. Concurrency and Computation: Practice and Experience, 37(12–14), Article e70129. https://doi.org/10.1002/cpe.70129

[23] Zhou, Y., Xu, J., Feng, T., Ma, X., Mu, J., & Pan, A. (2026). A theory of digital refocusing in Fourier ptychographic microscopy. APL Photonics, 11(5), Article 056110. https://doi.org/10.1063/5.0324237

[24] Kesgin, K., & Usta, E. (2026). Leakage-aware benchmarking and controlled ablation of attention models for student performance prediction across multiple tabular datasets. Discover Artificial Intelligence, 6, Article 1426. https://doi.org/10.1007/s44163-026-02398-3

[25] Fatoretto, M. B., Demétrio, C. G. B., Brophy, C., & de Andrade Moral, R. (2026). Bootstrap confidence intervals for generalized linear mixed models in dose-response analysis. Journal of Statistical Computation and Simulation, 96(14), 3630–3653. https://doi.org/10.1080/00949655.2026.2677023

[26] Ni, Y.-H., Fan, S.-Y., Zhang, S.-Y., & Sun, M.-J. (2024). Hyperuniform illumination subsampling method for Fourier ptychographic microscopy. Optics and Lasers in Engineering, 176, Article 108106. https://doi.org/10.1016/j.optlaseng.2024.108106

[27] Wu, K., Pan, A., Sun, Z., Shi, Y., & Gao, W. (2024). Blind deep-learning based preprocessing method for Fourier ptychographic microscopy. Optics & Laser Technology, 169, Article 110140. https://doi.org/10.1016/j.optlastec.2023.110140

[28] Espinosa-Momox, A., Norton, B., Serrano-García, D. I., & Porras-Aguilar, R. (2024). Dynamic quantitative phase microscopy: A single-shot approach using geometric phase interferometry. Communications Physics, 7, Article 256. https://doi.org/10.1038/s42005-024-01750-2